Journal of Alloys and Compounds 512 (2012) 316–322

Contents lists available at SciVerse ScienceDirect

Journal of Alloys and Compounds

journal homepage: www.elsevier.com/locate/jallcom

# Role of $Cr^{3+}$ ions on the microstructure development, and magnetic phase evolution of $Ni_{0.7}Zn_{0.3}Fe_2O_4$ ferrite nanoparticles

A.A. Birajdar[a], Sagar E. Shirsath[b,*], R.H. Kadam[c], S.M. Patange[c], K.S. Lohar[c], D.R. Mane[d], A.R. Shitre[e]

[a] Department of Physics, SMP Mahavidyalaya, Murum, Osmanabad (MS), India
[b] Department of Physics, Dr. Babasaheb Ambedkar Marathwada University, Aurangabad: 431 004 (MS), India
[c] Materials Research Laboratory, Srikrishna Mahavidyalaya Gunjoti, Omerga, Osmanabad 413613 (MS) India
[d] Department of Physics, Balbhim Mahavidyalaya, Beed (MS), India
[e] Department of Physics, YC Mahavidyalaya, Tuljapur, Osmanabad, (MS), India

ARTICLE INFO

*Article history:*
Received 24 May 2011
Received in revised form 4 September 2011
Accepted 28 September 2011
Available online 4 October 2011

*Keywords:*
Nanostructured materials
Sol–gel processes
Magentization
Magnetic measurements
Scanning electron microscopy, SEM

ABSTRACT

A series of ferrite samples with the chemical formula $Ni_{0.7}Zn_{0.3}Cr_xFe_{2-x}O_4$ ($x = 0.0–0.5$) were prepared by a sol–gel auto-combustion method and annealed at 600 °C for 4 h. The resultant powders were investigated by various techniques, including X-ray diffractometry (XRD), vibrating sample magnetometry (VSM), and permeability studies. The prepared samples have a cubic spinel structure with no impurity phase. As the $Cr^{3+}$ content $x$ increases, bulk density and crystallite size decrease, whereas porosity increases. The saturation magnetization decreases linearly from 58.31 to 42.90 emu/g with increasing $Cr^{3+}$ content. However, coercivity increases with increasing $Cr^{3+}$ substitution. The magnetic moments calculated from Neel's molecular-field model are in agreement in the experiment results. The initial permeability ($\mu_i$) decreases with increasing $Cr^{3+}$ substitution. The decrease in initial permeability ($\mu_i$) is attributed to decrease in magnetization on addition of $Cr^{3+}$. The real part of the permeability decreases gradually with increasing frequency in accordance with Snoek's law. The Curie temperature decreases linearly with increasing $Cr^{3+}$ content.

© 2011 Elsevier B.V. All rights reserved.

## 1. Introduction

Ni–Zn ferrites are one of the most versatile soft magnetic materials. Recently, the technological application of these materials has been studied extensively [1–4], primarily due to their applicability in many electronic devices owing to their high permeability at high frequency, remarkably high electrical resistivity, low eddy-current loss and reasonable cost [5–9]. The spinel structure of these ferrites possesses the general formula of $(A)[B_2]O_4$, where A represents cations in tetrahedral sites and B represents cations in the octahedral positions in a cubic structure. However, the formula $(A_{1-i}B_i)[AiB_{2-I}]O_4$ represents many possible intermediary distributions that denote considerable cation disorder, indicating that this structure requires special attention in terms of magnetic characterization [10]. The Ni–Zn ferrite is a well-known mixed inverse spinel [11] whose unit cell is represented by the formula $(Zn_xFe_{1-x})[Ni_{1-x}Fe_{1+x}]O_4$ [12,13], whereas the intrinsic magnetization (magnetic moment or total theoretical Bohr magneton of the lattice spinel) results from the inverse and normal phase, i.e., the distribution of cations in the spinel lattice. Based on these facts, the intrinsic magnetization of Ni–Zn ferrite can be calculated with and without the addition of 0.1 mol of chromium ions. Based on Hund's Rules [14], the magnetic moments of $Fe^{3+}$, $Cr^{3+}$, $Ni^{2+}$ and $Zn^{2+}$ are 5, 3, 2 and 0 $\mu_B$, respectively. The addition of impurities induces changes in the defect structure and texture of the crystal [15], creating significant modifications in the magnetic and electrical properties of these materials. Several researchers have studied the effects of $Cr^{3+}$ substitution in the spinel structure of ferrites [15–17]. However, we have not found any reports in the literature on Ni–Zn ferrite powders obtained by combustion reactions. Combustion synthesis, which is employed in the field of propellants and explosives, involves an exothermic and self-sustaining chemical reaction between the desired metal salts and a suitable organic fuel [18]. A key feature of the process is that the heat required to trigger the chemical reaction is provided by the reaction itself and not by an external source, such as urea [19]. Compared with other synthesis methods, the combustion-reaction process offers the advantages of being fast and simple without requiring subsequent intermediary calcination stages and consumes less energy during synthesis [20]. Like various other methods that have been proposed and applied in the preparation of ceramic powders, combustion synthesis allows for low-temperature synthesis, yielding products that are usually dry, crystalline, fine and chemically pure and homogeneous [21]. This paper therefore presents a study of nanosized Ni–Zn ferrite

---

* Corresponding author. Tel.: +91 02402240950: fax: +91 02402361270.
*E-mail address:* shirsathsagar@hotmail.com (S.E. Shirsath).

0925-8388/$ – see front matter © 2011 Elsevier B.V. All rights reserved.
doi:10.1016/j.jallcom.2011.09.087

doped with $Cr^{3+}$ produced by sol–gel auto-combustion synthesis and its morphologic, magnetic and permeability characterization.

## 2. Experimental

### 2.1. Synthesis method

The powders were synthesized by the sol-gel auto-combustion method. A.R. grade citric acid ($C_6H_8O_7 \cdot H_2O$), nickel nitrate ($Ni(NO_3)_2 \cdot 6H_2O$), zinc nitrate ($Zn(NO_3)_2 \cdot 6H_2O$), chromium nitrate ($Cr(NO_3)_3 \cdot 9H_2O$) and iron nitrate ($Fe(NO_3)_3 \cdot 9H_2O$) were dissolved in distilled water to obtain a mixed solution. The reaction procedure was carried out in an air atmosphere without the protection of inert gases. The molar ratio of metal nitrates to citric acid was 1:3. The metal nitrates were dissolved together in the minimum amount of double-distilled water needed to obtain a clear solution. An aqueous solution of citric acid was mixed with the metal-nitrate solution, and ammonia solution was slowly added to adjust the pH to 7. The mixed solution was placed on a hot plate with continuous stirring at 90 °C. During evaporation, the solution formed a very viscous brown gel. When all of the water molecules were removed from the mixture, the viscous gel began to froth. After a few minutes, the gel ignited and burnt with glowing flints. The decomposition reaction continued until the entire citrate complex was consumed. The auto-combustion was completed within a minute, yielding brown-colored ashes referred to here as the precursor. The prepared powders of all the samples were annealed at 600 °C for 4 h to obtain the final product. The powder was granulated using 2% PVA as a binder and pressed into discs and toroids (internal and outer diameters of 2 and 1 cm, respectively, and a thickness of 2 mm, with an applied pressure of 5000 kg/cm$^2$ to obtain the toroid-shaped samples for permeability measurements.

### 2.2. Characterization

The samples were powdered for X-ray investigation. One portion of the powder was examined using a Phillips X-ray diffractometer (Model 3710) with Cu-$K_\alpha$ radiation ($\lambda = 1.5405$ Å). The morphology and structure of the powder samples were studied using a JEOL-JSM-5600N scanning electron microscope (SEM). The magnetic measurements were performed at room temperature using a commercial PARC EG&G VSM 4500 vibrating sample magnetometer. The magnetic hysteresis loops were measured at room temperature with maximum applied magnetic fields of 0.8 T. The magnetic field sweep rate was 5 Oe/s for all measurements. The initial permeability ($\mu_i$) measurements on the toroid-shaped samples were conducted as a function of temperature and frequency. The initial permeability measurements of the toroid samples were taken using a HP-4284 A LCR precision meter.

## 3. Results and discussion

### 3.1. Structural analysis

The X-ray-diffraction (XRD) patterns of the $Ni_{0.7}Zn_{0.3}Cr_xFe_{2-x}O_4$ spinel ferrite system with $x = 0.0$–$0.5$ in steps of 0.1 are shown in Fig. 1. All of the Bragg peaks of the XRD patterns are broad and do not contain any extra peaks other than cubic spinel phase. The X-ray-diffraction analysis of these samples reveals the formation of single-phase cubic spinel structure.

The lattice constant '$a$' of all the samples was determined by using the equation discussed elsewhere [22]. The lattice-constant values were obtained for every sample using XRD data with an accuracy of ±0.002 Å and are listed in Table 1. The lattice constant initially increases and then begins to decrease. The initial increase of the lattice constant from $x = 0.0$ to 0.2 may be due to the fact that the substitution of $Cr^{3+}$ up to $x = 0.2$ does not affect the lattice. The decrease in the lattice constant above $x > 0.2$ is related to the difference in ionic radii of $Fe^{3+}$ and $Cr^{3+}$. In the present ferrite system, $Fe^{3+}$ ions (0.67 Å) ions are replaced by the relatively small $Cr^{3+}$ ions (0.64 Å). A similar nature was reported for other Cr-substituted spinel ferrites [23]. The X-ray density $d_x$ was calculated using the molecular weight and lattice constant. It can be seen from Table 1 that the X-ray density increases with increasing Cr content. The variation of the X-ray density with $x$ is opposite to that of the lattice constant with $x$ because the X-ray density is inversely proportional to the lattice constant. The average crystallite size ($t$) was determined using the line broadening of the most intense (3 1 1) diffraction peak using the Debye–Scherrer formula [22]. The values of the crystallite size are given in Table 1. The crystallite size is decreases from 35 nm to 20 nm with increasing $Cr^{3+}$ content. The specific surface area ($S$) was calculated from the diameter of the particle in nanometers and the measured density [24]. The values of surface area are given in Table 1. The specific surface ($S$) area increases with increasing $Cr^{3+}$ content. The increase in $S$ is due to the decrease in crystallite size.

**Table 1**
Lattice constant ($a$ and $a_{th}$), X-ray density ($d_x$), crystallite size ($t$), specific surface area ($S$), bulk density ($d_b$), porosity ($P$) and hopping lengths ($L_A$ and $L_B$) of $Ni_{0.7}Zn_{0.3}Fe_{2-x}Cr_xO_4$.

| Comp. $x$ | 0.0 | 0.1 | 0.2 | 0.3 | 0.4 | 0.5 |
|---|---|---|---|---|---|---|
| $a$ (Å) | 8.363 | 8.368 | 8.372 | 8.361 | 8.348 | 8.334 |
| $a_{th}$ (Å) | 8.422 | 8.418 | 8.414 | 8.41 | 8.406 | 8.402 |
| $d_x$ (Å) | 5.369 | 5.351 | 5.333 | 5.347 | 5.362 | 5.382 |
| $t$ (nm) | 35 | 32 | 29 | 25 | 22 | 20 |
| $S$ (m$^2$/gm) | 35.54 | 39.05 | 43.55 | 51.94 | 59.89 | 67.67 |
| $d_B$(g/cm$^3$) | 4.823 | 4.802 | 4.751 | 4.621 | 4.554 | 4.433 |
| $P$ (%) | 10.16 | 10.26 | 10.92 | 13.58 | 15.07 | 17.63 |
| $L_A$ (Å) | 3.621 | 3.623 | 3.625 | 3.62 | 3.615 | 3.609 |
| $L_B$ (Å) | 2.957 | 2.958 | 2.96 | 2.956 | 2.952 | 2.946 |

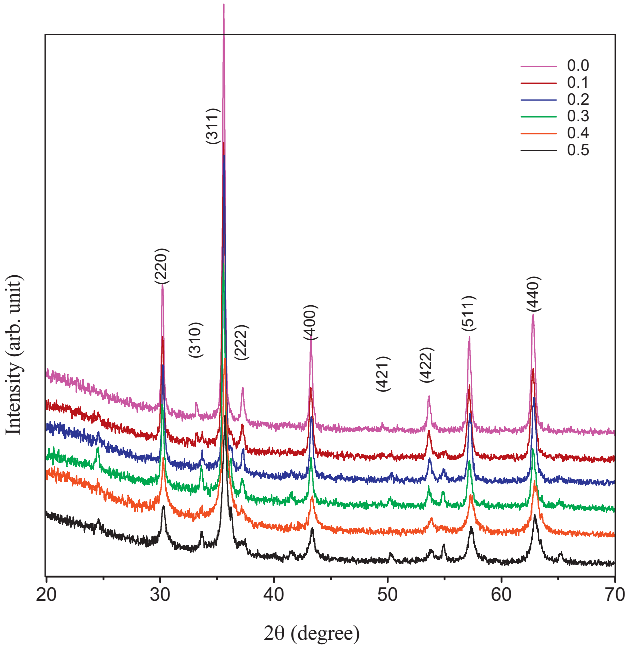

**Fig. 1.** X-ray diffraction patterns of $Ni_{0.7}Zn_{0.3}Cr_xFe_{2-x}O_4$.

The bulk density ($d_B$) of the specimens was determined by Archimedes' method. The values of the bulk density are shown in Table 1. The bulk density was found to decrease with increasing $Cr^{3+}$ content. In the present series, both the molecular weight of the $Ni_{0.7}Zn_{0.3}Fe_2O_4$ spinel ferrite and the volume of the unit cell decrease with increasing $Cr^{3+}$ substitution, but the rate of the decrease of the molecular weight is more than that of the volume. Therefore, the bulk density decreases with $Cr^{3+}$ substitution in the present case, which leads to an increase in porosity ($P$). The porosity of the ferrite nanoparticles was then determined using a relation discussed elsewhere [24]. The values of the percentage porosity are given in Table 1. It is clear from Table 1 that the sample density decreases and the porosity increases with increasing $Cr^{3+}$ content. The increase in porosity may be due the decrease in crystallite size, which increases the grain boundaries of the crystallite and accordingly the porosity. The increase in porosity can also be correlated with the decrease in bulk density of the samples with increase in $Cr^{3+}$ content. The high porosity values demonstrate the porous structure of the prepared Ni–Zn–Cr–Fe spinel ferrite samples.

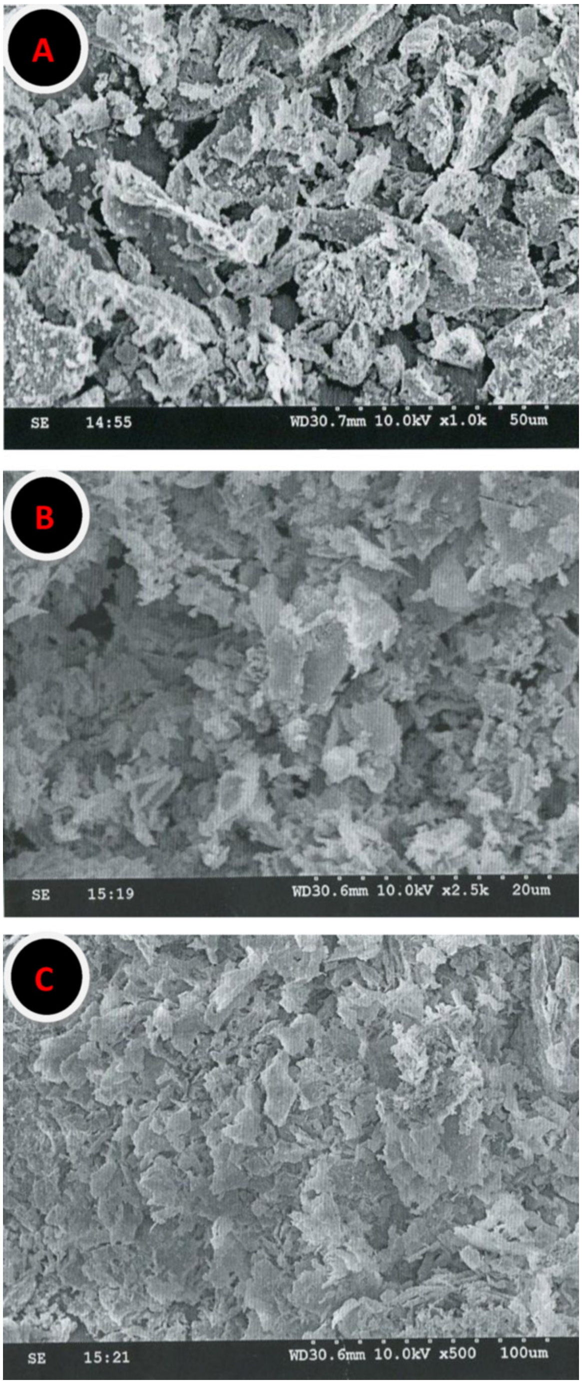

**Fig. 2.** SEM images for (A) $x = 0.2$, (B) $x = 0.3$ and (C) $x = 0.4$.

The hopping length ($L_A$ and $L_B$) between magnetic ions (the distance between the ions) in the tetrahedral A site and octahedral B site can be calculated using a relation discussed elsewhere [25]. The values of hopping lengths are given in Table 1, which shows that hopping length initially increases up to $x = 0.2$ and then decreases with further increases in $Cr^{3+}$ content. The results are explained by the variation in lattice constant with increasing $Cr^{3+}$ content.

The scanning electron micrographs for the typical samples ($x = 0.2$, 0.3 and 0.4) are shown in Fig. 2. It is evident from these figures that the microstructure of these samples is affected by $Cr^{3+}$ substitution.

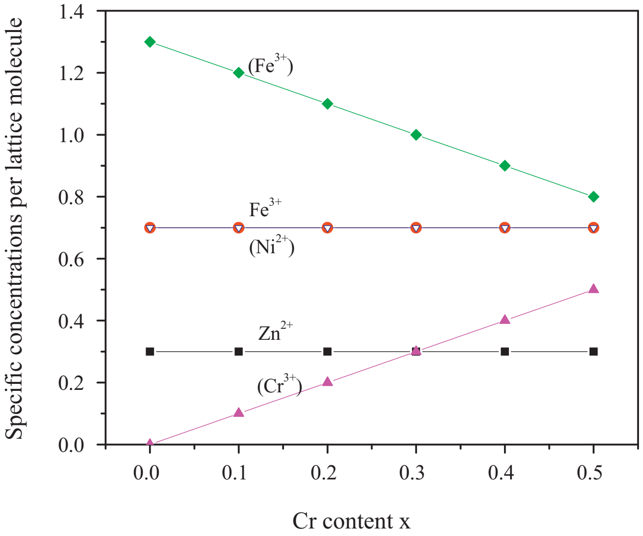

**Fig. 3.** Cation distribution calculated from XRD (parentheses enclose the octahedral ions).

The cation distribution in spinel ferrite can be obtained from an analysis of the X-ray diffraction pattern. In the present work, the Bertaut method [26] is used to determine the cation distribution. The cation distribution for each concentration and the site preferences of cations distributed among the tetrahedral A- sites and octahedral B- sites are presented in Fig. 3. In this figure, the fraction of $Fe^{3+}$ ions in either site is shown. The results demonstrate that $Ni^{2+}$ ions occupy B sites, whereas $Zn^{2+}$ ions occupy tetrahedral A sites. $Cr^{3+}$ preferentially replaces $Fe^{3+}$ from octahedral sites because of favorable crystal-field effects ($Cr^{3+} 6/5 \Delta_0$, $Cr^{3+} 0 \Delta_0$) [27]. It is observed from Fig. 3 that $Cr^{3+}$ ions predominately occupy the octahedral sites, which is consistent with the preference for large octahedral-site energy. With increasing $Cr^{3+}$ content, the fraction $Cr^{3+}$ ions in octahedral sites increases, whereas the fraction of $Fe^{3+}$ ions in octahedral sites decreases linearly.

The mean ionic radius of the A- and B-sites ($r_A$ and $r_B$) can be calculated using the relations discussed elsewhere [28,29]. The variation of $r_A$ and $r_B$ is shown in Fig. 4. It is shown that $r_A$ remains constant and $r_B$ decreases with increasing $Cr^{3+}$ content. The decrease in $r_B$ is due to the increasingly high occupation of the B site by the smaller ionic radii of $Cr^{3+}$ (0.64 Å), replacing $Fe^{3+}$ (0.67 Å). The theoretical values of the lattice parameter can be calculated with the help of an equation discussed elsewhere [30]. The

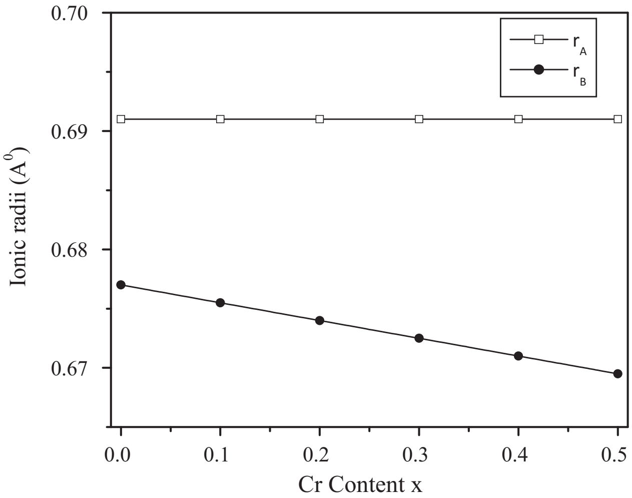

**Fig. 4.** Variation of ionic radii ($r_A$ and $r_B$) with Cr content $x$.

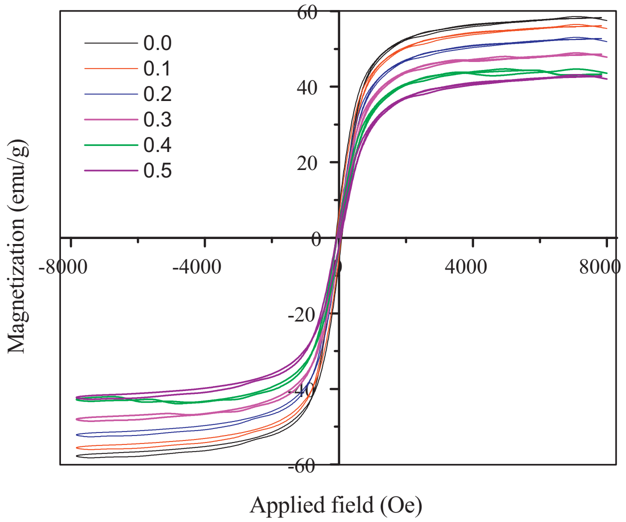

**Fig. 5.** Variation of magnetization with applied field.

values of theoretical lattice parameter $a_{th}$ are shown in Table 1. The variation of theoretical values is similar to that observed for the experimentally determined lattice parameter.

### 3.2. Magnetic analysis

The introduction of $Cr^{3+}$ ions into Ni–Zn ferrite greatly affects its magnetic properties. Fig. 5 shows the plots of the hysteresis loops for $Ni_{0.7}Zn_{0.3}Fe_{2-x}Cr_xO_4$ specimens. This figure indicates that Ni–Zn ferrite is a soft magnetic material with minimal hysteresis. The magnetic moment in ferrite is mainly due to the uncompensated electron spin of the individual ions and the spin alignments in the two sublattices, which are arranged in an antiparallel fashion. In a spinel ferrite, each ion at the A site has 12 B-site ions as nearest neighbors. According to Neel's molecular-field model [31], the A–B super-exchange interaction predominates the intrasublattice A–A and B–B interactions. Therefore, the net magnetic moment is given by the sum of the magnetic moments of the A and B sublattices.

The magnetic moment per formula unit ($n_B$) was calculated from Neel's sub-two-lattice model. For chromium-substituted Ni–Zn ferrite, the $Fe^{3+}$ ions are replaced by $Cr^{3+}$ ions, leading to a decrease in the B-site sublattice magnetization (Fig. 6). Therefore, the magnetization of the B sublattices decreases, which leads to a decrease in the net magnetization. The decrease in magneton number is explained by the A–B interaction. In the present case, $Cr^{3+}$ ions of low magnetic-moment values ($3\,\mu_B$) replace $Fe^{3+}$ ions of high magnetic moment ($5\,\mu_B$). According to the cation-distribution data from Fig. 3, $Cr^{3+}$ ions occupy octahedral B sites. This placement leads to a decrease of the magnetic moment of the B site, and thus the magneton number $n_B$ decreases with $Cr^{3+}$ concentration.

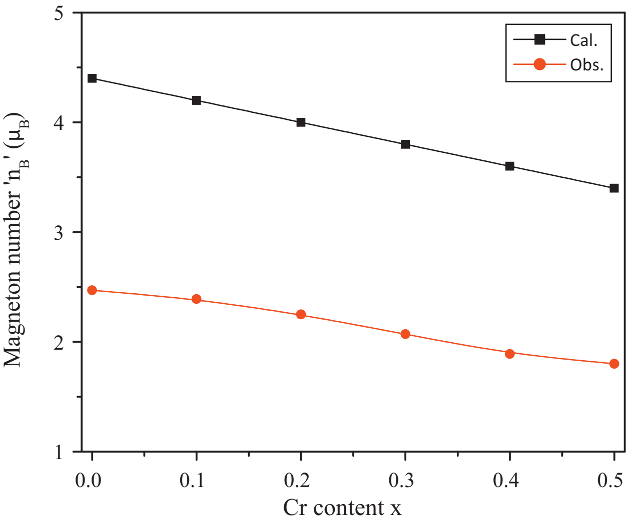

**Fig. 6.** Variation of magneton number with Cr content *x*.

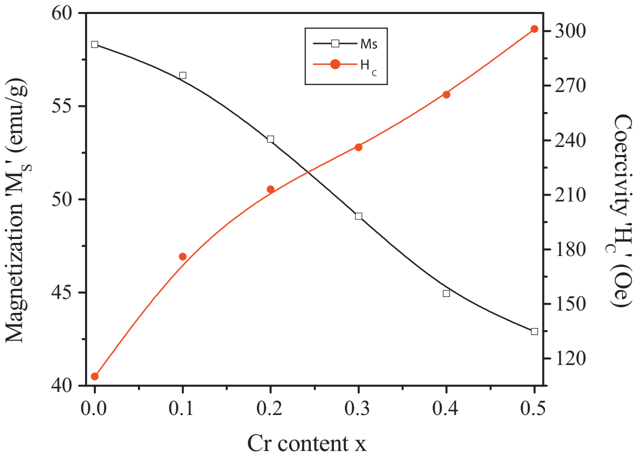

**Fig. 7.** Variation of magnetization and coercivity with Cr content *x*.

The magnetic moments calculated from Neel's molecular-field model are in agreement in the experiment results, which indicate that the saturation magnetization decreases monotonically with increasing Cr-substitution content (Fig. 7). The observed magnetic moment per formula unit in the Bohr magneton ($\mu_B$) was calculated using a relation discussed elsewhere [32]. The calculated and observed values of the magneton number are in close agreement, suggesting that the structure is collinear (Fig. 6). It has been established that the tetrahedral and octahedral sublattices of ferrite may be subdivided such that the resultant vector of the magnetic moments of the sublattices are aligned in such a direction that will influence the effective magnetization. Thus, the decrease in magnetization may be explained by the formation of a collinear spin arrangement due to the substitution of $Cr^{3+}$ ions.

The microstructure and homogeneity factors may also determine the magnetic properties. The small values obtained of the saturation magnetization can be due to microstructure with small particle size and others defects. For small particles the value of magnetization is significantly lower than the bulk value. The decrease in magnetization at small particle sizes is related with the effects of the relatively non-reactive surface layer that has low magnetization.

The coercivity ($H_c$) is an independent parameter, which can be altered by heat treatment or deformation and thus is independent of saturation magnetization. It is clearly observed from Fig. 7 that the coercivity increases as the $Cr^{3+}$ content increases, similarly to porosity. Porosity affects the magnetization process because the pores work as a generator of a demagnetizing field. As the porosity increases, a higher field is needed to push the domain wall, increasing $H_c$. The saturation magnetization is related to $H_c$ through Brown's relation [33]. According to this relation, $H_c$ is inversely proportional to $M_S$, which is consistent with our experimental results.

### 3.3. Permeability

#### 3.3.1. Thermal variation of permeability

The initial permeability measurements of toroid samples from room temperature to the Curie temperature at 1 kHz from low field

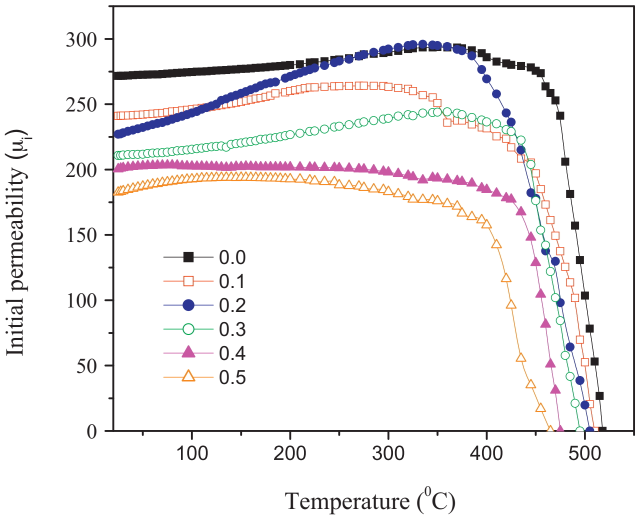

**Fig. 8.** Variation of initial permeability with temperature.

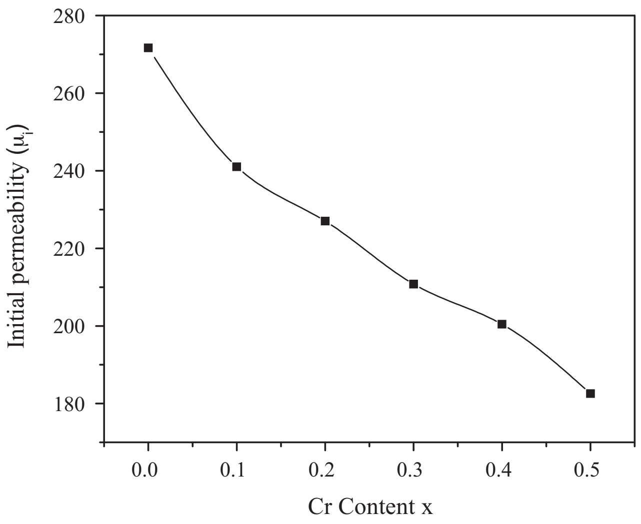

**Fig. 9.** Variation of initial permeability with Cr content *x*.

inductance measurements of coils with toroidal cores using the relation [34]:

$$\mu_i = \frac{L}{0.0046N^2h \ \log\left(\frac{d_2}{d_1}\right)} \tag{1}$$

where, $L$ is the inductance in μH; $N$ is the number of turns; $d_2$ is the outer diameter; $d_1$ is the inner diameter; $h$ is the height of core in cm; $\mu_i$ is the initial permeability.

The thermal and frequency variations of the initial permeability ($\mu_i$) provide valuable information about the domain nature [35], Curie temperature [36] and factors contributing to the permeability [37]. Many researchers [37–39] have explored the behavior of $\mu_i$ as a function of temperature. Parameters such as $M_s$, $D$ and $K_1$ are responsible for the diversity of the thermal spectra of $\mu_i$ for the ferrite sample. In present study, the variation of $\mu_i$ as a function of temperature in the range from room temperature to the Curie temperature are shown in Fig. 8.

For the compositions with $x = 0.0$, 0.1, 0.2 and 0.3,

- the initial permeability increases slowly with temperature and exhibits a peak near the Curie temperature, and
- near Tc, $\mu_i$ falls rapidly and it reaches zero at Tc. The sharp fall suggests the single-phase formation of the ferrite material.

Many researchers [40,41] have reported similar observations. The increase of $\mu_i$ with temperature can be explained as follows.

The anisotropy constant and saturation magnetization usually decrease with the increasing temperature due to thermal agitation, which disturbs the alignment of the magnetic moments [42]. However, the decrease of $K_1$ with temperature is much faster than that of $M_s$ [43]. When $K_1$ goes through zero, $\mu_i$ attains a maximum value and then drops to zero above Tc.

For compositions with $x = 0.4$ and 0.5,

- there is no peaking behavior in the $\mu_i$–$T$ variation,
- the permeability does not change with temperature up to a certain temperature,
- the initial permeability drops with temperature near Tc and becomes zero at Tc, and
- all of the compositions are single phase because a double Tc or a gradual variation of $\mu_i$ with $T$ was not observed.

The invariance of the initial permeability of these compositions up to a certain temperature is explained by considering the compensating effects of $M_s$ and $K_1$ with temperature. Kakatkar et al. [44] have reported $\mu_i$–$T$ curves for Ni–Zn ferrites and observed a very small decrease in $\mu_i$ over the temperature range of their experiment. They attributed this behavior to the compensating effects of $M_s$ and $K_1$ with temperature; however, the shape of the curves (except the magnitude of $\mu_i$) was not affected by the addition of $Cr^{3+}$. This behavior may be attributed to fact that the rate of change of $M_s$ and that of the anisotropy field with temperature is the same. This type of peak may be below the room-temperature region, and some researchers [45,46] have observed such a peak.

Thus, for these compositions, it can be concluded that the peaking behavior is absent due to the values of the anisotropy constant $K_1$, which do not change signs within the temperature range of the experiments.

### 3.3.2. Compositional variation in permeability

The compositional variation of the initial permeability ($\mu_i$) recorded at 298 K is shown in Fig. 9. The initial permeability ($\mu_i$) decreases with increasing $Cr^{3+}$ substitution. The observed variations of the initial permeability can be explained in terms of the Globus model [47]. According to this model, the initial permeability is dependent on the grain size, saturation magnetization and magnetocrystalline anisotropy.

The relationship between grain size and permeability is linear only if the grain growth is normal, i.e., if all grains grow at the same time and at the same rate. This limitation leads to a rather narrow range of final grain sizes. However, when some grains grow very rapidly, they trap pores, which can limit the permeability by pinning down the domain walls. When this exaggerated grain growth occurs, the porosity increases [48,49]. The initial permeability and saturation magnetization are two interdependent terms. The saturation magnetization was observed to decrease with increasing chromium content [50], and thus the observed variation can be correlated.

The Curie temperature (Tc) was obtained using the permeability curves ($\mu_i$–$T$). The variation of the Curie temperature with $Cr^{3+}$ content is shown in Fig. 10. The Curie temperature decreases linearly with increasing $Cr^{3+}$ content. This effect can be explained by the number of magnetic ions present in the two sublattices and their mutual interactions. In $Cr^3$-substituted Ni–Zn ferrite, the $Fe^{3+}$ ions are replaced by $Cr^{3+}$ ions at the B site. Because the magnetic moment of the $Cr^{3+}$ ions is 3 $\mu_B$, whereas the magnetic moment of

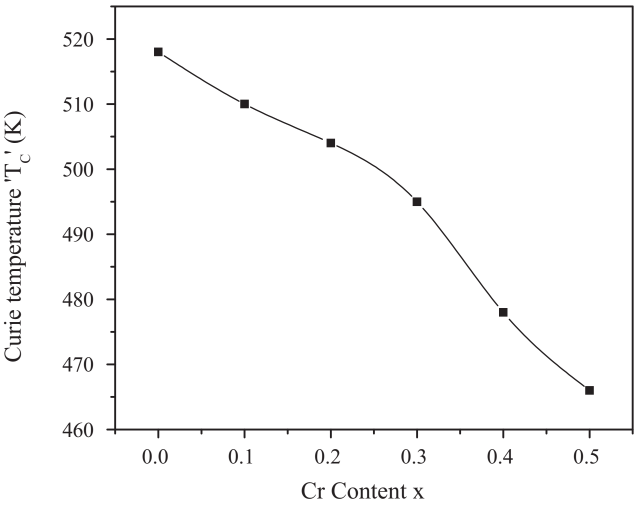

**Fig. 10.** Variation of Curie temperature with Cr content *x*.

the $Fe^{3+}$ ions is 5 $\mu_B$, an increase in the $Cr^{3+}$ concentration results in a reduction of the density of the magnetic ions. This decrease in turn results in a reduction of the net magnetic moment at the B sublattice, weakening the A–B exchange interaction of the type $Fe^{3+}$(A)–$O^{2-}$–$Fe^{3+}$(B). Because the Curie temperature is determined by the overall strength of the AB exchange interaction, the weakening of the $Fe^{3+}$(A)–$O^{2-}$–$Fe^{3+}$(B) interaction results in a decrease of the Curie temperature with successive increases in the $Cr^{3+}$ concentration of the Ni–Zn ferrites.

### 3.3.3. *Frequency variation of permeability*

The permeability of ferrite is mainly caused by spin rotation and domain wall displacement at microwave frequencies. When excited by an applied alternating magnetic field, the magnetization vector processes around the anisotropy field. According to previous works [51,52], in the presence of an external RF field, the real part $\mu_i'$ can be expressed as given in an equation discussed elsewhere [53]. As per this equation, when $\omega p > \omega$, $\mu_i'$ increases gradually as $\omega$ increases. When $\omega p = \omega$, a maximum in $\mu_i'$ is obtained, and when $\omega p > \omega$, the magnetization vector and the RF magnetic field become out of phase and $\mu_i'$ suddenly falls and becomes negative. This phenomenon is known as resonance. Resonance occurs when the frequency of the applied field coincides with the natural precessional frequency [54]. In Fig. 11, the real part of the permeability decreases gradually with increasing frequency. This result is in accordance with Snoek's law, which can be described by $f = (\gamma M_s/3\pi(\mu - 1))$[Hz], where $f$ is the resonant frequency, $M_s$ is the saturation magnetization, and $\gamma$ is the gyromagnetic ratio. The above-mentioned formula indicates that, because the resonant frequency is low, $\mu_i'$ will be high. The value of $\mu_i'$ depends significantly on the saturation magnetization. According to above-mentioned magnetization result, the net magnetization decreases gradually with increasing $Cr^{3+}$ content in chromium-substituted Ni–Zn ferrite. Therefore, the real part of the permeability of Ni–Zn ferrite is higher than that of chromium-substituted Ni–Zn ferrite.

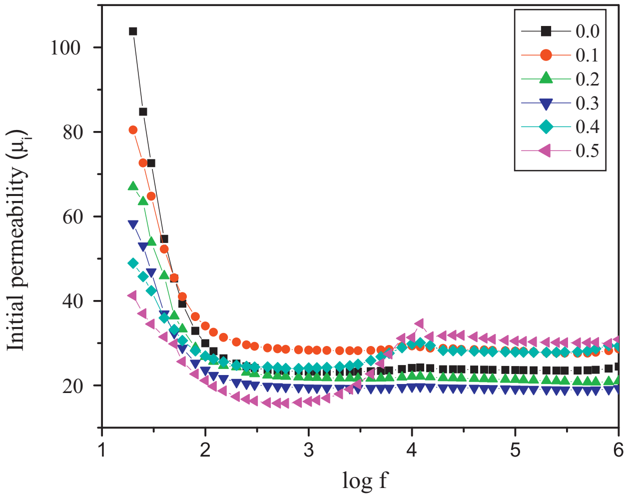

**Fig. 11.** Variation of real part of permeability with logarithm of frequency.

## 4. Conclusions

The substitution of $Cr^{3+}$ has induced significant changes in the structural and magnetic properties of Ni–Zn ferrite. Experimental results revealed that the lattice constant and cell initially increases and then decrease with increasing $Cr^{3+}$ content in Ni–Zn ferrite. The cation distribution suggests that $Cr^{3+}$ and $Zn^{2+}$ both have a strong preference towards the octahedral B site and that $Ni^{2+}$ also occupies the B site, whereas $Fe^{3+}$ occupies both the A and B sites. The calculated and observed values of the magneton number are in good agreement, suggesting that the structure is collinear. The saturation magnetization decreases linearly from 58.31 to 42.9 emu/g with increasing $Cr^{3+}$ content. This behavior is ascribed to the fact that the increasing concentration of nonmagnetic ions weakens the inter-site exchange interaction, decreasing the value of saturation magnetization. The crystallite size decreases from 35 nm to 20 nm with increasing $Cr^{3+}$ content. The initial permeability ($\mu_i$) decreases with increasing $Cr^{3+}$ substitution. The decrease in initial permeability ($\mu_i$) is attributed to decrease in magnetization on addition of $Cr^{3+}$. The real part of the permeability decreases gradually with increasing frequency in accordance with Snoek's law. Weakening of the $Fe^{3+}$(A)–$O^{2-}$–$Fe^{3+}$(B) interaction results in a decrease of the Curie temperature with successive increases in the $Cr^{3+}$ ions.

## References

[1] H. Igarash, K. Ohazaki, J. Am. Ceram. Soc. 60 (1997) 51.
[2] A. Goldman, Am. Ceram. Soc. Bull. 63 (1984) 582.
[3] A.M. Abdeen, J. Magn. Magn. Mater. 185 (1998) 199.
[4] B.V. Bhise, M.B. Dongare, S.A. Patil, S.R. Sawant, J. Mater. Sci. Lett. 10 (1991) 922.
[5] R.V. Mangalaraja, S. Ananthakumar, P. Manohar, F.D. Gnanam, Mater. Sci. Eng. A 355 (2003) 320.
[6] S. Zahi, M. Hashim, A.R. Daud, J. Magn. Magn. Mater. 308 (2007) 177.
[7] P.S. Anil Kumar, J.J. Shrotri, S.D. Kulkarni, C.E. Deshpande, S.K. Date, Mater. Lett. 27 (1996) 293.
[8] M.A. Ahmed, E. Ateia, L.M. Salah, A.A. El-Gamal, Mater. Chem. Phys. 92 (2005) 310.
[9] Y. Wang, F. Xu, L. Li, H. Liu, H. Qiu, J. Jiang, Mater. Chem. Phys. 112 (2008) 769–773.
[10] P.N. Lisboa-Filho, C. Vila, G. Petrucelli, C.O. Paiva-Santos, L. Gama, W.A. Ortiz, E. Longo, Physica B 320 (2002) 249.
[11] R.C. O'Handley, Modern Magnetic Materials-Principles and Applications, Wiley, USA, 2000.
[12] A.R. Bueno, L.C.F.L. Gomes, M.C.S. Nóbrega, Anais Congr. Brasileiro Cerâm. 41 (1) (1997) 135.
[13] A.S. Albuquerque, J. Ardisson, W.A.A. Macedo, Anais Congr. Brasileiro Cerâm. 41 (1) (1997) 142.
[14] S.M. Rezende, A Física de Materiais e Dispositivos Eletrônicos, Editora da Universidade Federal de Pernambuco, Recife, 1996, p. 392.
[15] A.M. El-Sayed, Mater. Chem. Phys. 82 (2003) 583.
[16] S.M. Patange, S.E. Shirsath, B.G. Toksha, S.S. Jadhav, K.M. Jadhav, J. Appl. Phys. 106 (2009) 023914.
[17] D.R. Mane, Swati Patil, D.D. Birajdar, A.B. Kadam, S.E. Shirsath, R.H. Kadam, Mater. Chem. Phys. 126 (2011) 755.
[18] A.C.F.M. Costa, E. Tortella, M.R. Morelli, M. Kaufman, R.H.G.A. Kiminami, J. Mater. Sci. 37 (2002) 3569.
[19] Y. Zhang, G.C. Stangle, J. Mater. Res. 9 (1994) 1997.
[20] Z. Lou, J. Hao, Thin Solid Films 450 (2004) 334.
[21] S.E. Shirsath, R.H. Kadam, A.S. Gaikwad, A. Ghasemi, A. Morisako, J. Magn. Magn. Mater. 323 (2011) 3104.
[22] B.D. Cullity, Elements of X-Ray Diffraction, Addison-Wesley Publ. Comp. Inc, Reading, Massachusetts, U.S.A, 1956, p. 99.

[23] S.M. Patange, S.E. Shirsath, B.G. Toksha, S.S. Jadhav, S.J. Shukla, K.M. Jadhav, Appl. Phys. A: Mater. Sci. Process. A95 (2009) 429.
[24] I.H. Gul, A.Z. Abbasi, F. Amin, M. Anis-Ur Rehman, A. Maqsood, J. Magn. Magn. Mater. 311 (2007) 494.
[25] B. Vishwanathan, V.R.K. Murthy, Ferrite Material Science and Technology, Narsoa Publishing House, New Delhi, 1990.
[26] L. Weil, E.F. Bertaut, L. Bochirol, J. Phys. Radium 11 (1950) 208.
[27] A. Tomas, P. Laruelle, J.L. Dormann, M. Nouges, Acta Crystallogr. C39 (1983) 1615.
[28] M.A. Amer, Hyp. Interact. 131 (2000) 29.
[29] S.E. Shirsath, B.G. Toksha, R.H. Kadam, S.M. Patange, D.R. Mane, G.S. Jangam, A. Ghasemi, J. Phys. Chem. Solids 71 (2010) 1669.
[30] R. Valenzuela, Magnetic ceramics, Cambridge University Press, 1994.
[31] L. Neel, Ann. Phys. 3 (1948) 137.
[32] S.E. Shirsath, S.S. Jadhav, B.G. Toksha, S.M. Patange, K.M. Jadhav, J. Appl. Phys. 110 (2011) 013914.
[33] J.M.D. Coey, Rare Earth Permanent Magnetism, John Wiley and Sons, New York, 1996.
[34] N.D. Chaudhari, R.C. Kambale, J.Y. Patil, S.R. Sawant, S.S. Suryavanshi, Mater. Res. Bull. 45 (2010) 1713.
[35] C.R.K. Murthy, S.D. Likhite, E.J. Deutch, G.S. Murthy, Phys. Earth Planet Int. 30 (1982) 287.
[36] S.R. Jadhav, S.R. Sawant, S.S. Suryavanshi, S.A. Patil, J. Less Commun. Met. 158 (1990) 199.
[37] S.A. Mazen, S.F. Mansour, H.M. Zaki, Cryst. Res. Technol. 38 (2003) 471.
[38] E. Rezlescu, N. Rezlescu, C. Posnicu, M.L. Crauss, Ceram. Int. 19 (1993) 71.
[39] N. Rezlescu, E. Rezlescu, Solid State Commun. 88 (1993) 139.
[40] A.M. Sankapal, S.V. Kakatkar, N.D. Chaudhari, R.S. Patil, S.S. Suryavanshi, S.R. Sawant, J. Mater. Sci.-Mater. Electron. 9 (1998) 173.
[41] S.S. Bellad, S.C. Watwe, B.K. Chaugule, J. Magn. Magn. Mater. 195 (1999) 57.
[42] S.S. Bellad, B.K. Chaugule, Mater. Res. Bull. 33 (1998) 1165.
[43] K. Ohta, J. Phys. Soc. Jpn. 18 (1963) 685.
[44] S.V. Kakatkar, S.S. Kakatkar, R.S. Patil, A.M. Sankpal, N.D. Chaudhari, P.K. Maskar, S.S. Suryavanshi, S.R. Sawant, Mater. Chem. Phys. 46 (1996) 96.
[45] S.A. Morrison, C.L. Cahill, E.E. Carpenter, S. Calvin, R. Swaminathan, M.E. Mottenry, V.G. Haris, J. Appl. Phys. 95 (2004) 6392.
[46] C. Caizer, M. Stefanescu, J. Phys. D: Appl. Phys. 35 (2002) 3035.
[47] A. Globus, P. Duplex, M. Guyot, IEEE Trans. Magn. Magn. 7 (1971) 617.
[48] E.C. Snelling, A.D. Giles, Ferrites for Inductors and Transformers, Research Studies Press, 1983, p. 38.
[49] J. Zhu, K.J. Tseng, IEEE Trans. Magn. Magn. 40 (2004) 3339.
[50] R. Laishram, S. Phanjoubam, H.N.K. Sarma, C. Prakash, J. Phys. D: Appl. Phys. 32 (1999) 2151.
[51] A. Verma, D.C. Dube, J. Am. Ceram. Soc. 88 (2005) 519–523.
[52] A.J. Moulson, J.M. Herbert, Electroceramics: Materials, Properties and Applications, Chapman & Hall, London, 1990, p. 247.
[53] Y.-P. Fu, D.-S. Hung, Y.-D. Yao, Ceram. Int. 35 (2009) 2179.
[54] V.R.K. Murthy, S. Sundaram, B. Viswanathan, Microwave Materials, Narosa Publishing House, New Delhi, 1994, p. 143.